

Article

Research on the Fast Charging Strategy of Power Lithium-Ion Batteries Based on the High Environmental Temperature in Southeast Asia

Qin Zhang * and Yuyang Yu

College of Smart Transportation Modern Industry, Anhui Sanlian University, Hefei 230601, China;
yyy@mail.slu.edu.cn

* Correspondence: 18160882206@163.com

Abstract: To address the problem of excessive charging time for electric vehicles (EVs) in the high ambient temperature regions of Southeast Asia, this article proposes a rapid charging strategy based on battery state of charge (SOC) and temperature adjustment. The maximum charging capacity of the cell is exerted within different SOCs and temperature ranges. Taking a power lithium-ion battery (LIB) with a capacity of 120 Ah as the research object, a rapid charging model of the battery module was established. The battery module was cooled by means of a liquid cooling system. The combination of the fast charging strategy and the cooling strategy was employed to comprehensively analyze the restrictions of the fast charging rate imposed by the battery SOC and temperature. The results indicate that when the coolant flow rate was 12 L/min and the inlet coolant temperature was 22 °C, the liquid cooling system possessed the optimal heat exchange capacity and the lowest energy consumption. The maximum temperature (T_{max}) of the battery during the charging process was 50.04 °C, and the charging time was 2634 s. To lower the T_{max} of the battery during the charging process, a charging rate limit was imposed on the temperature range above 48 °C based on the original fast charging strategy. The T_{max} decreased by 0.85 °C when charging with the optimized fast charging strategy.



Academic Editor: Ottorino Veneri

Received: 27 October 2024

Revised: 10 December 2024

Accepted: 20 December 2024

Published: 25 December 2024

Citation: Zhang, Q.; Yu, Y. Research on the Fast Charging Strategy of Power Lithium-Ion Batteries Based on the High Environmental Temperature in Southeast Asia. *Batteries* **2025**, *11*, 5. <https://doi.org/10.3390/batteries11010005>

Copyright: © 2024 by the authors. Licensee MDPI, Basel, Switzerland. This article is an open access article distributed under the terms and conditions of the Creative Commons Attribution (CC BY) license (<https://creativecommons.org/licenses/by/4.0/>).

1. Introduction

In response to the crisis of the continuous depletion of oil resources, the development of EVs has emerged as an important initiative. The Southeast Asia region is mainly situated in the tropics, where the average annual temperature is generally within the range of 25 °C to 30 °C [1]. The suitable temperature is conducive to the popularization of EVs. Consequently, countries in the Southeast Asia region have generally initiated an electrification transformation. Among them, the 30@30 policy formulated by the Thai government aims to achieve an output of zero-emission EVs exceeding 30% of the total vehicle output by 2030 [2]. Furthermore, the Thai government will also establish a special fund to offer price subsidies to consumers who purchase EVs. The Malaysian government is facilitating the electrification transformation by enhancing the investment in charging infrastructure for EVs. As indicated by the memorandum signed by the Malaysian Automotive Importers and Traders Association, the installation density of direct current (DC) charging piles across the entire nation of Malaysia is expected to reach 30 per 10,000 km² by 2025 [3]. The Indonesian government has responded actively to the plans for reducing greenhouse gas

emissions, putting forward the goal of achieving zero emissions by 2060. In the policy of the electrification transformation of transportation formulated in 2022, the Indonesian government proposed that the annual output of EVs should reach 1 million by 2035 [4]. Most of the power sources adopted by EVs are power LIBs [5]. However, the charging speed of power LIBs is influenced by the battery temperature. Generally, the higher the temperature, the slower the charging rate [6]. The charging process of EVs in the Southeast Asia region is predominantly influenced by high ambient temperatures for the majority of the time, resulting in prolonged charging periods. Consequently, it is indispensable to develop a rapid charging strategy under conditions of high ambient temperatures (with an ambient temperature of 40 °C).

Research on the fast charging strategies of EVs under high ambient temperatures typically needs to be combined with battery cooling systems. Liu et al. (2024) investigated the cyclic charge and discharge strategies of LIB modules at high ambient temperatures based on a hybrid scheme combining phase change material cooling and liquid cooling. The results indicate that the hybrid cooling scheme can offer relatively good temperature uniformity. Under the conditions of 3 C discharge and 1 C charge in the cycle, the maximum temperature difference of the battery modules is controlled within 3 °C [7]. In the most recent research, the non-destructive fast charging strategy for avoiding lithium plating has emerged as a research hotspot. The lithium-free charging strategy mainly regulates the current during the charging process to maintain the battery temperature within the lithium plating boundary. Yu et al. (2024) investigated the charging methods for suppressing lithium plating by establishing a second-order RC equivalent circuit model of the battery. The results indicate that after optimization by the particle swarm algorithm considering the suppression of lithium dendrites, when the ratio of the lithium suppression weight coefficient to the temperature rise weight coefficient is 3:7, the charging time of the battery is the shortest and the maximum temperature rise is the lowest [8]. The fast charging strategy under high environmental temperatures is intended to solve issues such as overly long charging duration and battery overheating during the charging process.

The battery fast charging strategy was established based on the relationship among SOC, temperature, and charging rate, with the objective of exploiting the maximum charging capacity of the cell. High-rate battery charging, especially under high ambient temperatures, gives rise to a significant amount of heat. Consequently, an efficient battery thermal management system is indispensable. Currently, the battery thermal management systems of commercial EVs are mainly liquid cooling systems, while a small portion adopt air cooling systems and direct cooling systems with refrigerants [9,10]. The air-cooling system possesses advantages such as low cost and easy maintenance, and was extensively applied in the early stage of the development of EVs [11]. Nevertheless, the cooling performance of the air cooling system is only applicable to battery systems with relatively low heat generation and fails to satisfy the cooling requirements under high-rate charging. The direct cooling system injects the refrigerant utilized for air conditioning cooling directly into the battery system via the compressor, capable of extracting a considerable amount of heat within a short period [12]. Structurally, the direct cooling system reduces pipeline distribution compared to the liquid cooling system and is highly integrated with the vehicle's heat pump system. However, its structural design is rather complex, and there exists the risk of refrigerant leakage. Furthermore, the regulation algorithm of refrigerant flow and the implementation strategies for supercooling and superheating are rather intricate, resulting in this system not being widely applied. Liquid cooling systems possess advantages such as high thermal conductivity efficiency and excellent temperature uniformity [13]. Therefore, they have currently emerged as the prevailing commercial solutions. Guo et al. (2022) investigated the influences of the structural parameters and

the flow rate of the serpentine channel on the thermal performance of a battery based on orthogonal experiments [14]. The results indicated that the liquid cooling plate with the parallel helical serpentine channel exhibited superior heat dissipation performance. The optimized parallel channels demonstrated a considerable improvement in pressure drop, with a 74.18% reduction in pressure drop compared to the initial design. Zhao et al. (2023) devised a honeycomb-structured liquid cooling plate with the aim of augmenting the heat exchange area of the cooling channels [15]. Experiments were designed and numerical computations were carried out with the structural parameters of the liquid cooling plate and the inlet flow rate of the coolant as variables. The results indicated that an increase in the inlet flow velocity can ameliorate the maximum temperature and the maximum temperature difference of the battery. However, when the flow velocity exceeds 0.3 m/s, the improvement in temperature is not notable. The combination of an efficient liquid cooling system and a fast charging strategy can bring into play the maximum charging capacity of LIBs and greatly shorten the charging time of EVs.

The battery liquid cooling system adopted in this paper refers to the commercially available serpentine stamping liquid cooling plate. On this basis, a fast charging strategy based on battery SOC and temperature regulation is proposed. Firstly, the thermal physical parameters of the lithium-ion power battery were acquired through the Hybrid Pulse Power Characterization (HPPC) test, and the heat generation model of the battery was established. Subsequently, numerical simulations of battery fast charging were conducted based on the proposed battery fast charging strategy and cooling strategy. By adjusting the inlet flow rate and the inlet coolant temperature to investigate their influences on the charging performance, an optimized strategy of restricting the charging rate in the high-temperature range was proposed. Finally, the optimized fast charging strategy was experimentally verified. The fast charging strategy and the cooling strategy proposed in this paper are capable of exerting the maximum charging rate (3.2 C) of the cell. The battery SOC takes 2654 s to be fully charged from 0% to 100%, and the maximum temperature of the battery throughout the fast charging process is 49.19 °C. This fast charging strategy can not only reduce the charging time of large-capacity batteries in high ambient temperatures but also enhance the safety during the charging process.

2. Models and Methods

2.1. Physical Model and Parameters

For the convenience of numerical calculation, the structure of the battery pack fabricated in this research was simplified. As shown in Figure 1, the overall envelope dimensions of the battery pack are 1366.3 × 1166 × 142.9 mm. The battery pack consists of three modules, and the assembly mode of each module is 1P36S, while that of the battery pack is 1P108S. Insulating sheets are arranged at the end plates on both sides of the module along the Y direction to prevent short circuits between the cells and enhance the safety of the battery system. During the charging and discharging processes, the heat generation of the cells exhibits a phenomenon of heat accumulation towards the middle. Therefore, an insulating frame was deployed between the cells to attain the effect of blocking heat transfer. When the cooling of the battery system is activated, the coolant enters the cold plate from the inlet and undergoes heat exchange with the battery module through the cold plate to achieve the purpose of cooling the cells. To enhance the heat transfer efficiency between the cold plate and the module and minimize the impact of contact thermal resistance, three heat conducting pads were placed at the contact surface. The upper cover of the battery pack is connected to the housing by bolts, and the gasket is arranged on the contact surface. The waterproof and dustproof grade of the battery pack reaches IP68 (6 indicates no dust

ingress; 8 indicates sustainable immersion without water ingress). The thermal physical parameters of each component structure of the battery pack are presented in Table 1.

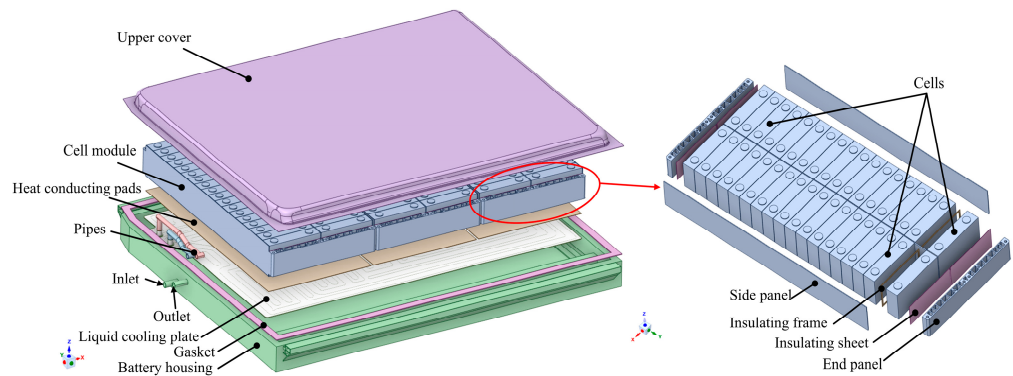


Figure 1. Structural model of battery pack.

Table 1. Thermal physical parameters of the battery pack structure.

Structure	Material	Density (kg/m ³)	Specific Heat Capacity (J/kg·K)	Thermal Conductivity (W/m·K)
Upper part housing	steel	7800	480	58
Thermal pad	mixtures	2200	2100	1.5
Pipe	nylon	1030	1800	0.16
Liquid cooling plate	Al	2730	893	167
Gasket	silica gel	360	920	0.07
Battery housing	Al	2730	893	167
Cell	mixtures	2165	966	12.3/3.2/10.1(x/y/z-direction)
Side panel	Al	2730	893	167
Insulating frame	silica gel	433	1175	0.04
Insulating sheet	PP + PET	1200	1170	0.2
End panel	Al	2730	893	167

2.2. Battery Model

2.2.1. Coolant Model

To simplify the calculations, the following assumptions are applicable to this study:

1. The thermal physical parameters of each component structure of the battery pack remain constant;
2. Thermal radiation is ignored during the cooling process [16];
3. The fluid is incompressible [17].

In this study, the coolant adopted was a 50% concentration ethylene glycol deionized aqueous solution. Based on the above assumptions, the momentum conservation equation, energy conservation equation, and continuity equation of the coolant are as follows [18,19]:
momentum conservation:

$$\rho_c (\vec{v} \cdot \nabla \cdot \vec{v}) + \nabla \cdot P = \mu \nabla^2 \vec{v} \quad (1)$$

where ρ_c , \vec{v} , P , and μ are the density, velocity vector, static pressure, and dynamic viscosity of the coolant, respectively.

energy conservation:

$$\rho_c c_c (\vec{v} \cdot \nabla \cdot T_c) = k_c \nabla^2 T_c \quad (2)$$

where c_c , T_c , and k_c are the specific heat capacity, temperature, and thermal conductivity of the coolant, respectively.

Continuity equation:

$$\frac{\partial \rho_c}{\partial t} + \nabla \cdot (\rho_c \cdot \vec{v}) = 0 \quad (3)$$

2.2.2. Heat Generation Model

During the high-rate charging process of LIBs, complex chemical reactions occur internally and are accompanied by the generation of heat. Specifically, the heat production within LIBs mainly originates from four components: the heat of chemical reactions, the heat of side reactions, Joule heat, and polarization heat [20]. The heat of chemical reactions mainly refers to the heat resulting from the entropy change of internal electrochemical reactions. The generation of the heat of side reactions exists concomitant with the physical changes within the battery, for instance, the rupture of the solid electrolyte interphase (SEI) film. The heat of side reactions is only generated when the battery experiences thermal runaway and can be negligible under normal charging conditions [21]. The generation of Joule heat and polarization heat are attributed to the ohmic resistance and polarization resistance within the battery, respectively.

During the charging process of LIBs, the heat generated internally is conducted to the outside via diffusion, and the heat conservation equation is as follows [22]:

$$\rho c_b \frac{\partial T}{\partial t} = \nabla \cdot (k \nabla T) + q \quad (4)$$

where q is the heat generation rate per unit volume.

The heat generation within a LIB can be expressed as follows [23]:

$$Q_g = Q_r + Q_j + Q_p \quad (5)$$

where Q_g is the heat generation of the battery, and Q_r , Q_j , and Q_p denote the chemical reaction heat, Joule heat, and polarization heat inside the battery, respectively.

Substituting the ohmic internal resistance and polarization internal resistance into Equation (5) yields the following:

$$Q_g = I^2(R_e + R_p) + IT \frac{\partial U_{OCV}}{\partial T} \quad (6)$$

where R_e and R_p denote the ohmic internal resistance and polarization internal resistance of the battery, respectively. U_{OCV} is the open-circuit voltage of the battery.

The ohmic internal resistance and the polarization internal resistance are collectively referred to as the battery internal resistance, and Equation (6) can again be expressed as follows:

$$Q_g = I^2(R_b) + IT \frac{\partial U_{OCV}}{\partial T} \quad (7)$$

where R_b is the internal resistance of the battery.

The heat produced by the internal electrochemical reaction of the LIB during the charging process is mainly transferred through heat conduction, heat convection, and heat radiation [24]. Among them, the calculation of heat radiation is based on the Stefan–Boltzmann theorem, and its result is very small and can be disregarded [25]. Therefore, the primary heat transfer modes are the former two.

1. Heat conduction

The heat transfer within the battery presents a regularity: it flows from the high-temperature zone to the low-temperature zone until the temperature is balanced.

During the heat transfer process, the component structures inside the battery are stable, and the macroscopic displacement can be neglected. It can be regarded that the microscopic particles within transfer energy during their movement. The expression is as follows [26]:

$$Q_1 = -kA \frac{dt}{dx} \quad (8)$$

where A represents the heat exchange area, and $\frac{dt}{dx}$ is the temperature gradient.

2. Heat convection

The thermal energy within a LIB is conducted to the exterior through a fluid medium, and the energy transfer of this process can be computed in accordance with Newton's law of cooling:

$$Q_2 = -hA\Delta T \quad (9)$$

where h is the heat transfer coefficient, and ΔT denotes the temperature difference between the battery and the fluid.

2.3. The Calculation Method of Battery Heat Generation

The cells adopted in this study are square LIBs with a rated capacity of 120 Ah, which are manufactured by JIANGSU ZHENGЛИ New Energy Battery Technology Co., Ltd. Suzhou City, China. The detailed specifications of the battery cells are presented in Table 2.

Table 2. Parameters of LIB.

Item	Specification	Notes
Rated capacity	120 Ah	25 °C & 1/3 C
Rated voltage	3.22 V	25 °C & 1/3 C
Mass	2.05 kg	/
Operating temperature	Discharge: -30~55 °C Charge: -20~55 °C	/
Maximum current allowed for continuous charging	384 A	3.2 C
Dimensions	44.0 × 194.5 × 114.5 mm	Thickness × Width × Height

It can be known from the battery heat generation model in Section 2.2.2 that the main factors influencing the heat generation of the battery are the internal resistance and the OCV (open-circuit voltage). The voltage variation data of the battery during the charging and discharging processes can be acquired through the HPPC test, and thereby the internal resistance can be calculated [27]. The aim of the HPPC test lies in determining the dynamic power capacity of a cell under current pulse working conditions. During the test, the main attention is paid to the 10 s charging power and the 10 s discharging power. The experimental equipment for the HPPC test is shown in Figure 2, mainly encompassing a high-power charging and discharging system (BAT-NEH 1000 V, FUJIAN XINGYUN Electronics Co., Ltd., Fuzhou City, China), a high- and low-temperature control box (JW-1502, SHANGHAI JUWEI Instrument Equipment Co., Ltd., Shanghai City, China), a battery module, a data acquisition system (P-CAN, Darmstadt Peak System Technology Co., Ltd., Darmstadt, Germany), and a computer. Among these, the maximum charging power of the charging and discharging system is 600 kW, and the maximum continuous charging current is 600 A. The temperature control box can provide the required temperature in the range -60 °C~80 °C. The testing method employed in this research refers to the previous research conducted by Landini et al. (2021) [28]. The testing steps are as follows:

1. Battery Discharge: When the battery temperature is left to stabilize at 25 °C, it is discharged to SOC = 0% at a rate of 0.33 C.

2. Standstill: The battery is left in standstill for 1 h after discharging to ensure it reaches an equilibrium state.
3. Constant Current Pulse Test: A constant charging pulse current is imposed on the battery for a duration of 10 s, with the pulse current implemented in accordance with Table 3. Subsequently, the battery is left at rest for 30 s. Next, a constant discharging current pulse is applied to the battery for 10 s, and the pulse current is executed as per Table 3.
4. SOC Node: After each pulse, the battery is charged at 0.33 C to the next SOC node, and the operations of steps 1 and 3 are repeated. The interval between each SOC node is 10%.
5. Stop: Charging ceases when the SOC is charged to 100% at a rate of 0.33 C.

Table 3. Charging and discharging current pulse.

SOC (%)	3	5	10	20	30	40	50	60	70	80	90	95	100
Charging rate (C)	/	4.26	4.26	3.6	3.25	2.79	2.35	2.13	1.87	1.70	1.45	1.29	/
Discharging rate (C)	2.20	2.86	4.25	5.26	5.26	5.26	5.26	5.26	5.26	5.26	5.26	/	5.26

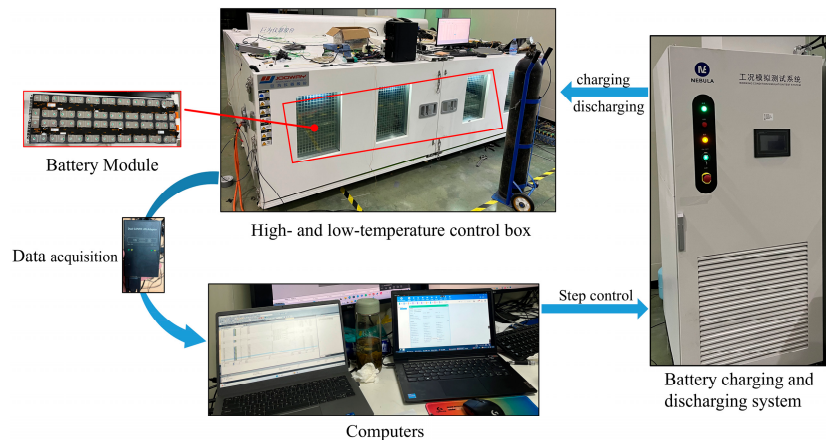


Figure 2. Experimental platform for charging and discharging test.

Throughout the testing process, the battery voltage at each period of rest is recorded to construct the open circuit voltage (OCV) curve of the battery, as depicted in Figure 3. The procedure of the battery internal resistance test is illustrated in Figure 4. After a charging pulse is imposed on the battery, the voltage instantaneously rises from V_a to V_b , and then ascends to V_c as the charging concludes. The voltage variation characteristics depicted in Figure 4 can be interpreted as the instantaneous elevation of the voltage plateau by the ohmic internal resistance, and the slow rise of the voltage plateau during the charging process attributed to the polarization internal resistance [29]. During the charging process, the heat output of the battery is simultaneously influenced by the ohmic internal resistance and the polarization internal resistance. In this research, the internal resistance of the battery was computed based on the voltage variation in the charging pulse phase, and the expression is as follows:

$$R_b = \frac{(V_c - V_a)}{I} \quad (10)$$

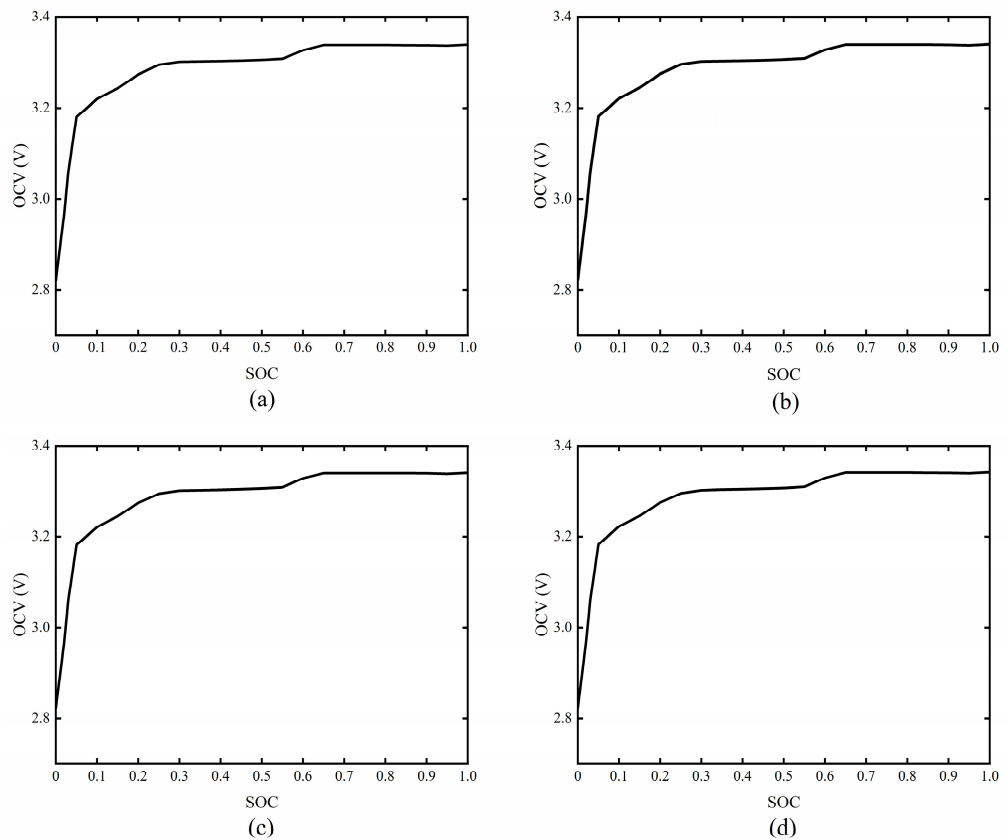


Figure 3. The OCV curves of battery at different temperatures: (a) 20 °C; (b) 30 °C; (c) 40 °C; (d) 50 °C.

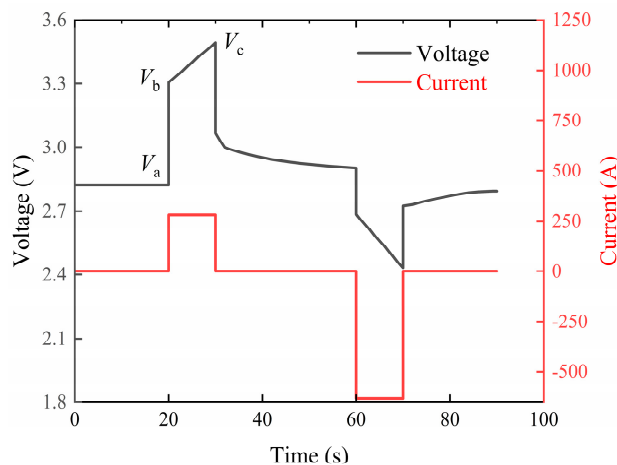


Figure 4. Evolution of the voltage and current in an HPPC cycle step.

2.4. Numerical Methods

As depicted in Figure 1, the upper cover and the battery housing are in a state of natural convection with the air, and the heat transfer coefficient is $5 \text{ W}/(\text{m}^2 \cdot \text{K})$. The initial conditions are as follows:

- Inlet: Flow inlet. The coolant flow rate is 12 L/min, and the coolant temperature at the inlet is 22 °C;
- Outlet: Pressure outlet. $P_{out} = 0 \text{ Pa}$.
- Ambient temperature: 40 °C.

The meshing of the battery pack computational domain is carried out using polyhedral meshes, as depicted in Figure 5. Specifically, in order to improve the accuracy of the

simulation of convective heat transfer in the fluid–solid coupling region, two layers of boundary layer with a total thickness of 1 mm were set in the coupling region. The calculation formula of the Reynolds number is as shown in Equation (11). The inlet Reynolds number was calculated to be 14,182 based on the flow velocity. Therefore, the flow state of the coolant is turbulent, and the K-Epsilon model was selected as the turbulence model. Considering the accuracy and computational cost of the numerical model, the maximum number of internal iterative steps was set to 10 at the beginning of the calculation and then to 2 when the calculation tended to be stable. The transient calculation method was adopted for the numerical simulation:

$$R_e = \frac{\rho v d}{\mu} \quad (11)$$

where R_e is the Reynolds number, v is the fluid velocity, and d represents the pipe diameter.

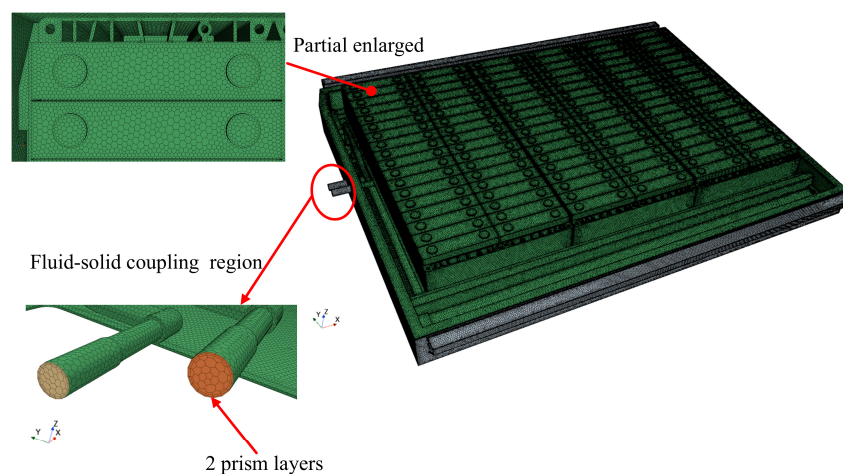


Figure 5. The mesh model of battery pack.

2.5. Fast Charging Strategy

The battery fast charging strategy is designed to exert the maximum charging power of the cell under different SOCs and temperatures. The charging power of the battery is jointly determined by the voltage platform of the battery pack and the requested current. The aim of this study lies in applying the battery fast charging strategies to different cell platforms. Owing to the variations in the rated capacities of different cells, the fast charging strategy represented by current is not instructive. Hence, the fast charging strategy proposed in this study is based on the battery SOC-temperature-charging rate, and is illustrated in Figure 6. The maximum charging power of the cell adopted in this study is 3.2 C (384 A). The principal factors influencing the charging performance of the cell are SOC and temperature. During the process of fast charging, with the increase in SOC, the polarization phenomenon within the battery intensifies, leading to an increase in the internal resistance of the battery [30]. A rise in battery temperature will intensify the internal chemical reaction rate, resulting in an augmentation of the thermal stress within the battery. There is a risk of thermal runaway for batteries when they are charged at a high rate under conditions of high SOCs and temperatures. Therefore, the fast charging strategy needs to set distinct maximum allowable charging rates in accordance with different temperature and SOC intervals. As shown in Figure 6, the charging rate was restricted within the interval where the SOC is higher than 80% and the temperature is higher than 50 °C. When the battery is within the range of low SOC and low temperature, the maximum charging rate of the cell

should be exerted. The charging rate is gradually decreased as the SOC and temperature increase, as shown in Region I in Figure 6. The charging rate undergoes stepwise transitions.

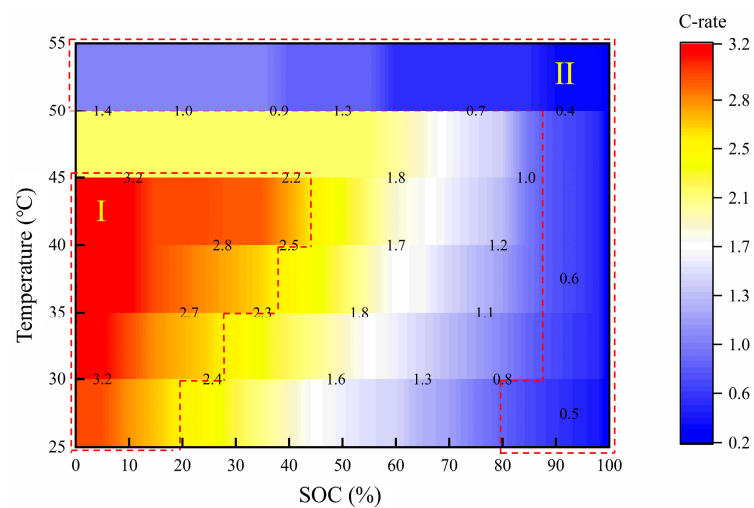


Figure 6. The fast charging strategy of batteries.

2.6. Cooling Strategy

The fast charging strategy significantly shortens the charging time by enhancing the charging rate. Nevertheless, a considerable amount of heat is produced within the battery during the fast charging process. If not cooled promptly, it will lead to a rapid increase in the battery temperature, thereby influencing the charging efficiency and safety. Therefore, through the cooling strategy, the battery temperature can be effectively controlled within the safety boundary. The setting of the temperature threshold in the battery cooling strategy is crucial for ensuring the operation of the battery pack within a safe and efficient temperature range. In this study, a mature and commercially available liquid cooling battery thermal management system was adopted. The temperature threshold settings for the activation and deactivation of the liquid cooling system are as follows:

- The liquid cooling system is activated: The maximum battery temperature is $\geq 38\text{ }^{\circ}\text{C}$; inlet coolant temperature: $22\text{ }^{\circ}\text{C}$; coolant flow rate: 12 L/min;
- The liquid cooling system is deactivated: The maximum battery temperature is $\leq 33\text{ }^{\circ}\text{C}$.

3. Results and Discussion

3.1. Charging Performance

For the charging performance of batteries in high ambient temperatures, we mainly paid attention to two indicators: battery temperature and charging time. The battery module is cooled by means of the battery thermal management system to achieve the goal that the battery does not exceed the temperature limit. The excessive charging time of batteries is one of the crucial factors restricting the popularity of EVs, and the fast charging strategy is designed to address such issues. According to the different charging habits of EV users, they can be roughly divided into the following two usage scenarios [31].

1. Urban Areas and Workday Utilization: A large number of charging piles are available, and the majority of users opt to charge their batteries when the SOC is 10%.
2. Highways and Long-Distance Utilization: The number of service areas equipped with charging facilities is scarce and the distances between adjacent ones are considerable. Users would choose to charge when the SOC is 30%.

It needs to be additionally explained that the majority of users will select home charging piles for charging when using in urban areas instead of public paid charging piles. In the usage scenario of highways, users can only choose to conduct paid charging at service areas.

3.1.1. Charging Time

This section discusses numerical computations conducted for the rapid charging process of the battery. Figure 7a presents the variations of battery temperature, current, and SOC during the rapid charging process. The variation of the current with time exhibits a stepwise decreasing trend. The magnitude of the current is jointly regulated by the SOC and temperature. After the charging commences, the current is charged at the maximum capacity of 384 A (3.2 C). When the charging proceeded to 103 s, the battery temperature exceeded 45 °C, and the current was immediately reduced to 254 A (2.12 C) for charging. At this moment, the SOC was 9.2%, and the current reduction was due to temperature regulation. When the charging proceeded to 359 s, the battery temperature exceeded 50 °C. At this moment, the current decreased to 120 A (1 C) for charging. Low-rate charging leads to a relatively small amount of heat generation in the cell. Therefore, the battery thermal management system is capable of cooling the battery temperature to below 50 °C within an extremely short period. Subsequently, the current was augmented to 254 A for charging. With the increase in the current, the T_{max} of the battery reached 50 °C again promptly. Therefore, within the charging time period ranging from 359 s to 1397 s, the T_{max} of the battery hovered around 50 °C. The current is subject to temperature regulation and remains in a fluctuating state, as depicted in Figure 7. When charging reached 1398 s, the SOC was 65%, and the current was adjusted to 222 A (1.85 C) for constant current charging. At this point, the current is regulated by the SOC. With the decline in the charging rate, the battery temperature commenced to decrease after 1398 s. Within the charging time period spanning from 1398 s to 2634 s, the current descended from 222 A stepwise to 60 A (0.5 C). At 1855 s (the SOC is 85%), the charging current experienced a considerable drop, from 168 A to 108 A. This is primarily attributed to the implementation of a current-limiting strategy at a high SOC. The entire charging process (the SOC is charged from 0 to 100%) lasts for 2634 s.

Figure 7b depicts the variations of current and T_{max} during the charging process of the battery SOC from 10% to 80%. The initial charging current is 384 A (3.2 C), and it decreases to 360 A (3 C) at 57 s, with the SOC being 15%. As the charging proceeds, the T_{max} of the battery reaches 50 °C at 379 s. Subsequently, under the effect of the cooling system, the battery temperature hovers around 50 °C. After charging until 1159 s, the battery temperature starts to decline gradually, and the SOC at this moment is 66%. The time taken for the battery SOC to charge from 10% to 80% is 1460 s.

Figure 7c presents the alterations in current and T_{max} throughout the charging process of the battery SOC from 30% to 80%. In contrast to Figure 7a,b, when the battery commences charging from 30% SOC, the initial current is 354 A (2.95 C). The charging current is relatively lower at the initial stage, and the temperature rise rate of the battery is also lower. Consequently, the battery charging current remains at 254 A (2.12 C) during the time period from 142 s to 428 s. When the battery SOC is charged to 58%, the T_{max} of the battery attains 50 °C. Subsequently, the current fluctuates within the SOC range of 58% to 69%. The entire charging process lasts for 955 s.

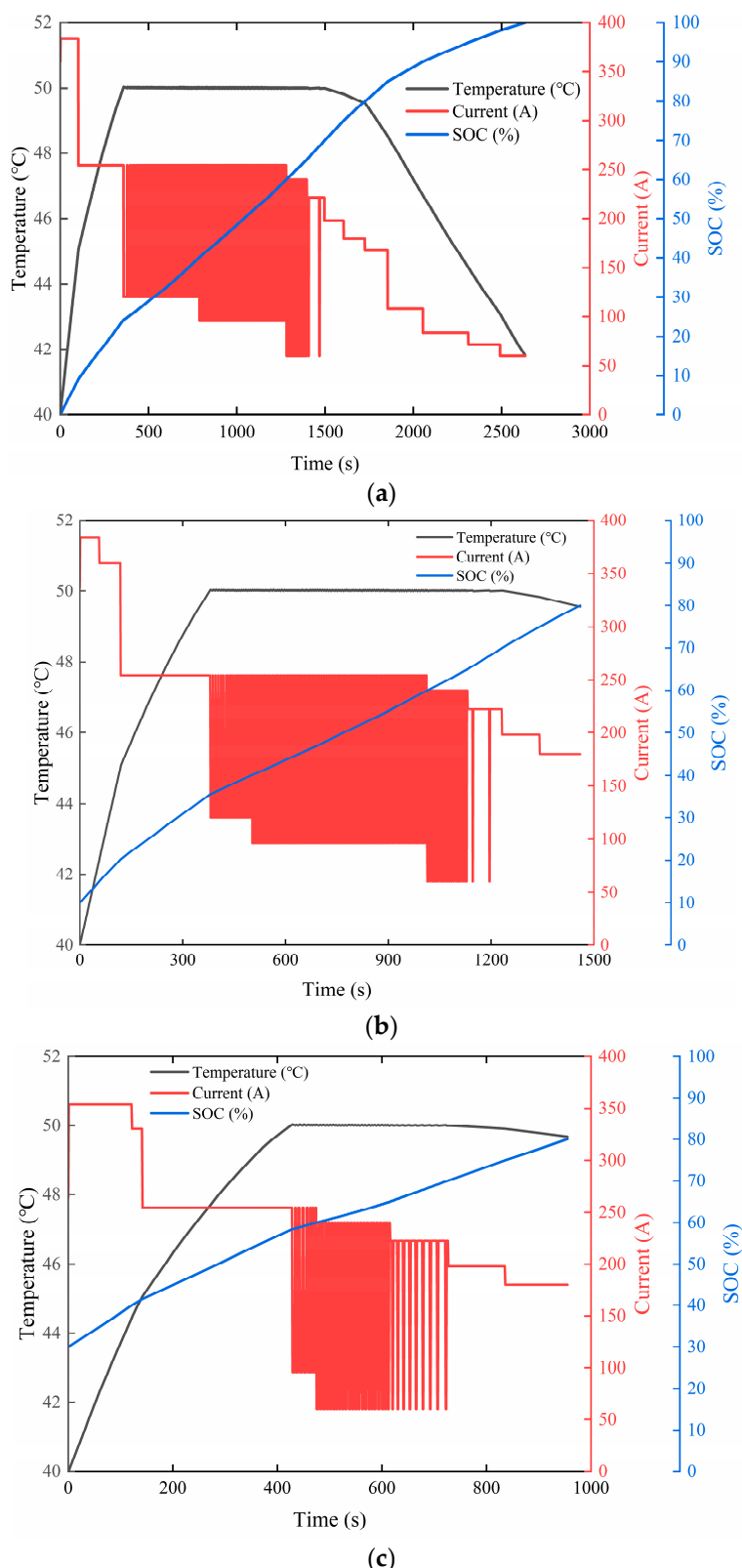


Figure 7. Comparison of fast charging performance in different SOC intervals: (a) Temperature, current, and SOC changes of 0–100% SOC charging; (b) temperature, current, and SOC changes of 10–80% SOC charging; (c) temperature, current, and SOC changes of 30–80% SOC charging.

3.1.2. Battery Temperature

The variation of the charging rate in the fast charging strategy is regulated in accordance with the battery SOC and the T_{max} . The data of the battery SOC were directly

extracted from the data acquisition system. The battery pack in this study comprises 108 cells, and it is infeasible to extract the temperature of each individual cell during the charging process. Therefore, several representative cells were chosen within the high-temperature and low-temperature aggregation areas of the battery, and negative temperature coefficient thermistors (NTC) were arranged on the top surfaces of these cells to collect the temperature. As depicted in Figure 8, a total of 12 NTCs were arranged within the battery pack.

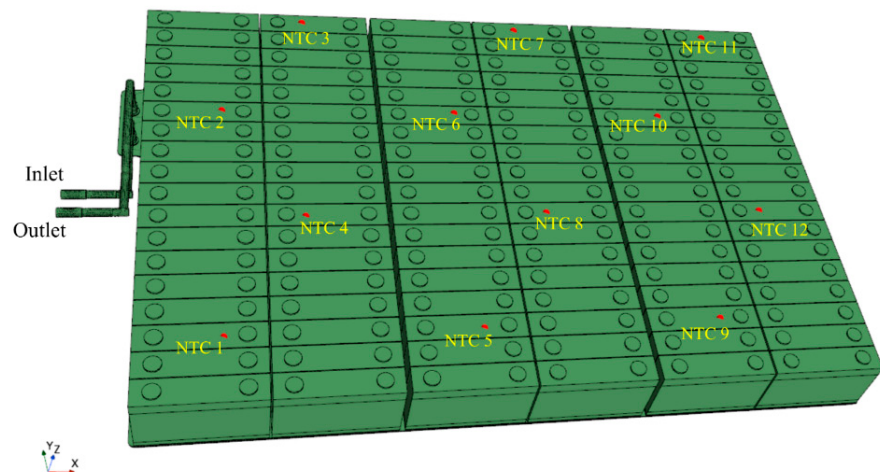


Figure 8. The position of NTC in the battery pack.

The fast charging strategy depicted in Figure 6 exploits the maximum charging capacity of the cells at the initial stage of charging. With the advancement of charging, the battery temperature exhibits a continuous upward tendency. As illustrated in Figure 9, the variation curves of the NTC temperature during the charging process in three distinct SOC intervals are presented. When the battery temperature exceeds 50°C , the current rate is restricted to below 1 C, and at this point, the heating power of the cell is approximately 15 W. As the battery is in a low-rate charging status, the battery thermal management system is capable of cooling the battery rapidly. When the battery temperature drops to below 50°C , the charging rate of the battery rises to 2.12 C. At this time, the heat output of the battery augments, and the battery temperature promptly exceeds 50°C once more. Consequently, there exists a fluctuation interval of the battery temperature curve at 50°C . As depicted in Figure 9a, when the charging proceeded to 357 s, the T_{\max} of the battery surpassed 50°C , attaining 50.01°C . Subsequently, the T_{\max} fluctuated around 50°C for 1050 s. Similarly, the temperature fluctuation phenomenon also emerged in the charging processes with the initial SOCs being 10% and 30%, as illustrated in Figure 9b,c. During the process of the battery SOC being charged from 0 to 100%, the T_{\max} of the battery was 50.04°C , and the maximum temperature difference was 4.34°C . In the battery temperature curve depicted in Figure 9, the SOC intervals corresponding to the temperature fluctuations are 24% to 65%, 35% to 65%, and 58% to 69%, respectively. The fast charging strategy illustrated in Figure 6 implements a rate restriction in the high SOC interval (greater than 85%). Consequently, the temperature fluctuation intervals depicted in Figure 9 are all within the range where the battery is capable of conducting high-rate charging. To enhance the charging speed under high ambient temperatures, it is essential to lower the T_{\max} of the battery during the charging process.

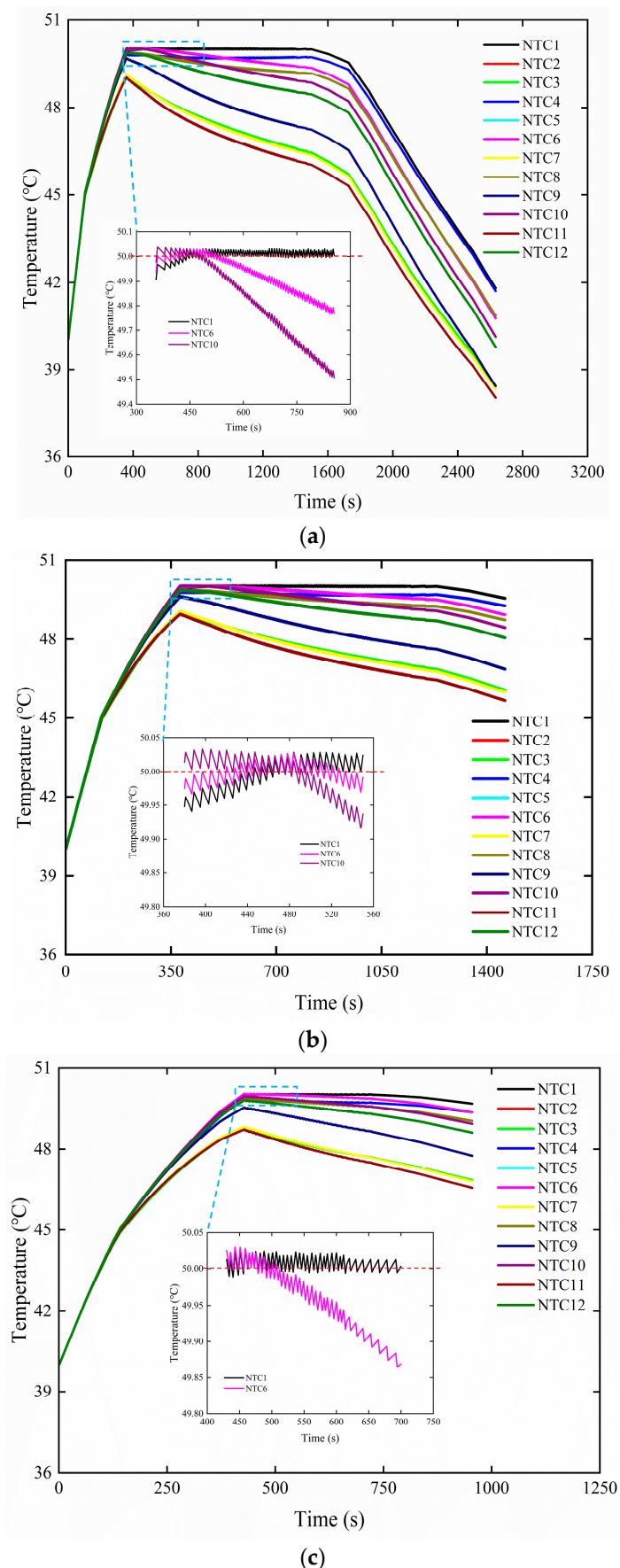


Figure 9. Comparison of NTC temperatures at different SOC charging intervals: **(a)** SOC: 0–100%; **(b)** SOC: 10–80%; **(c)** SOC: 30–80%.

3.2. The Influence of Cooling Strategies on Charging Performance

EVs undergo rapid charging under high ambient temperatures, and the battery modules are cooled by means of a thermal management system. The liquid cooling system initiates and terminates the cooling operation based on the battery temperature thresholds. As indicated by the highest temperature curve in Section 3.1.2, the liquid cooling system remains active throughout the charging process. The temperature and flow rate of the coolant at the inlet are implemented in accordance with the strategy described in Section 2.6. To improve the heat exchange capacity of the battery liquid cooling thermal management system, the heat exchange amount of the system can be increased by adjusting the cooling strategy.

3.2.1. The Influence of Inlet Flow Rate

The heat transfer capacity of the liquid cooling system can be adjusted through the inlet flow rate. Specifically, when the inlet temperature of the coolant remains unchanged, enhancing the inlet flow rate of the coolant can boost the cooling capacity of the liquid cooling system. In this section, the rapid charging process of the battery with inlet flow rates of 12 L/min and 15 L/min was numerically simulated. Figure 10 presents the variation curves of battery temperature and cold plate pressure drop under the two inlet flow rates. As depicted in Figure 10b, when the inlet flow rate is elevated to 15 L/min, the T_{max} of the battery during the charging process is 50.04 °C, the maximum temperature difference of the battery is 4.48 °C, and the maximum pressure drop is 45,373 Pa. In comparison with the inlet flow rate of 12 L/min, the increase in the inlet flow rate did not bring about an improvement in the T_{max} of the battery. Instead, the increase in the inlet flow rate reduced the temperature uniformity of the cooling system. In terms of charging time, when the inlet flow rate is 15 L/min, the entire charging process lasts for 2609 s. The reduction in charging time is mainly because when the T_{max} of the battery is within the fluctuation range, the heat generated by the cells can be quickly removed. When the inlet flow rate is raised from 12 L/min to 15 L/min, the fluctuation time of the T_{max} of the battery is reduced by 37 s. Furthermore, with the increase in the inlet flow rate, the maximum pressure drop of the liquid cooling system rises by 44%.

3.2.2. The Influence of the Inlet Coolant Temperature

The liquid cooling system can also improve the cooling capacity by reducing the inlet coolant temperature. This section describes the numerical simulation of the battery charging process when the inlet coolant temperature is 20 °C and the inlet flow rate is 12 L/min. The charging processes of three SOC intervals were simulated, and the data of battery temperature and charging time are presented in Figure 11. During the charging process of the battery SOC from 0% to 100%, the T_{max} of the battery is 50.04 °C, and the entire fast charging process lasts for 2585 s. It can be observed from the temperature curves presented in Figure 9a–c that the decrease in the inlet coolant temperature did not notably ameliorate the battery temperature. Nevertheless, the charging times were reduced by 49 s, 37 s, and 22 s, respectively. Likewise, the improvement in the charging time can be interpreted as the reduction in the fluctuation time of the T_{max} .

Consequently, in conjunction with the analysis in Section 3.2.1, it can be concluded that the cooling strategy formulated in Section 2.6 of this study can bring into play the maximum cooling performance of the liquid cooling system.

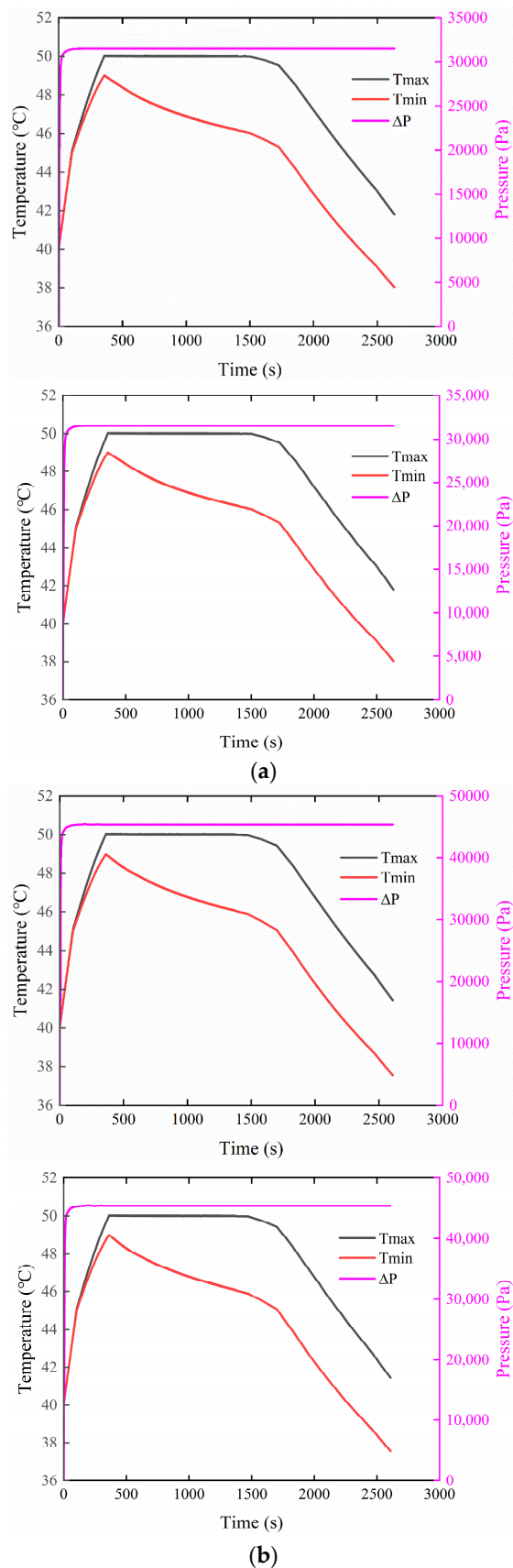


Figure 10. Comparison of charging performance under different inlet flow rates: (a) 12 L/min; (b) 15 L/min.

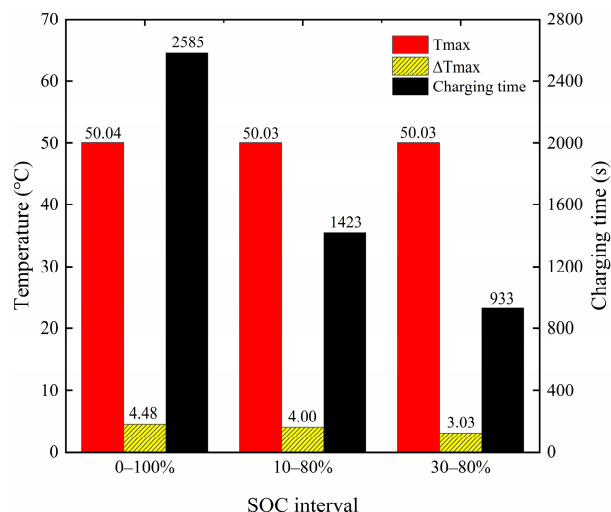


Figure 11. Comparison of charging performance at different SOC intervals under the inlet coolant temperature of 20 °C.

3.3. The Optimization of the Fast Charging Strategy

The battery thermal management system employed in this study exerted its maximum capacity when implementing the cooling strategy. Therefore, to reduce the T_{max} of the battery during the charging process, a temperature limit for the charging rate in the fast charging strategy is necessary. As depicted in Figure 6, when the T_{max} range of the battery lies between 45 °C and 50 °C, the charging rate employed for charging the SOC from 0% to 60% is 2.12 C. During this charging stage, the average heating power per cell is 48 W. The liquid cooling system is capable of suppressing the temperature rise rate of the battery at this stage, but fails to maintain the T_{max} of the battery below 50 °C. The initial SOCs for the temperature fluctuations depicted in Figure 9a–c are 24%, 35%, and 58%, respectively, precisely falling within the range where the charging rate is 2.12 C. Consequently, in this section, a charging rate limitation is imposed on the temperature range from 48 °C to 50 °C based on the original fast charging strategy, as illustrated in Figure 12. Specifically, when the T_{max} of the battery exceeds 48 °C, the charging rate is decreased from the original 2.12 C to 1.5 C. The decrease in the charging rate leads to a reduction in the heating power of the battery. Therefore, when the T_{max} of the battery exceeds 48 °C, the liquid cooling system is capable of better controlling the temperature rise of the battery.

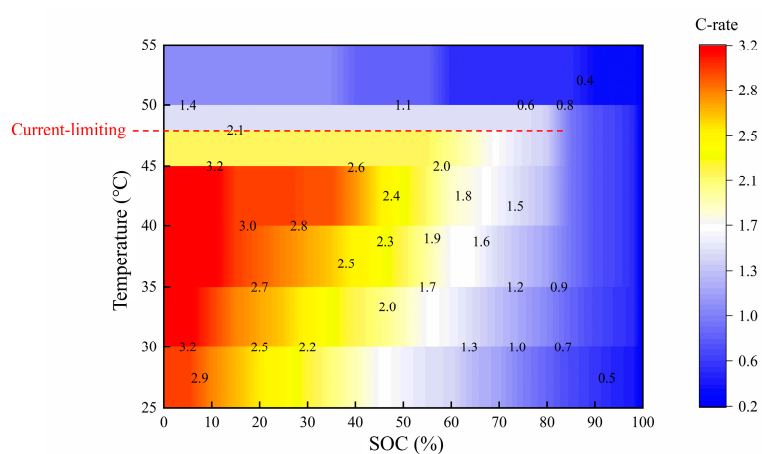


Figure 12. Optimized fast charging strategy.

3.3.1. Comparison of Charging Performance

This section describes numerical simulations performed on the optimized fast charging strategy, and the cooling strategy is implemented as described in Section 2.6. Figure 13 presents the numerical results of the charging process in three distinct SOC intervals. It can be observed from Figure 13a that when the charging proceeds to 240 s, the T_{max} of the battery attains 48 °C. Subsequently, the charging current was decreased from 254 A (2.12 C) to 180 A (1.5 C). Within the charging time period ranging from 241 s to 1745 s, the charging rate remained at 1.5 C. During the charging process, the T_{max} of the battery is consistently maintained below 50 °C. This phenomenon indicates that the optimized fast charging strategy is effective in restraining the T_{max} of the battery. As depicted in Figure 13a–c, the T_{max} values of the battery are 49.19 °C, 49.08 °C, and 48.93 °C, respectively. The maximum temperatures of the battery are reduced by 0.85 °C, 0.95 °C, and 1.10 °C, respectively, compared to the original fast charging strategy. As illustrated in Figure 13a–c, the charging processes for the three SOC intervals consumed 2654 s, 1495 s, and 1005 s, respectively. The charging times increased by 20 s, 35 s, and 50 s, respectively, compared to the original fast charging strategy. The increase in charging time can be accounted for by the limitation of the charging rate. The charging process depicted in Figure 13a–c has durations when the T_{max} of the battery exceeds 48 °C of 1530 s, 1237 s, and 720 s, respectively. Moreover, when the T_{max} of the battery is higher than 48 °C, the SOC is consistently below 80%. In other words, the charging rate remains at 1.5 C within the range where the battery overheats. The prolonged low-rate charging results in an increase in the charging time.

To investigate the influence of cooling strategies on the optimized fast charging strategy, in this section, the charging process with an inlet coolant temperature of 20 °C and a coolant flow rate of 15 L/min was numerically simulated. Furthermore, the charging process of the original fast charging strategy under the same conditions was numerically simulated. As depicted in Figure 14a,b, through the methods of reducing the inlet coolant temperature and increasing the coolant flow rate, the maximum temperatures of the battery were decreased by 0.32 °C, 0.33 °C, and 0.34 °C in the three charging processes, respectively. Similarly, the charging times were reduced by 62 s, 46 s, and 1 s, respectively. However, the increase in flow rate resulted in an increase in the pressure drop of the liquid cooling system. As depicted in Figure 15, when the cooling strategy was altered from 22 °C@12 L/min to 20 °C@15 L/min, the pressure drop of the liquid cooling system rose by 13,670 Pa. From the aspect of pressure drop, the improvement in the optimized cooling strategy on battery temperature and charging time was not significant. As shown in Figure 14, the optimized fast charging strategy does not have an advantage in charging time compared to the original fast charging strategy. However, the T_{max} of the battery can be maintained below 50 °C, which has a positive effect on battery thermal safety and cell life.

3.3.2. Experimental Validation

To validate the accuracy of the numerical model employed in this research, a fast charging experiment of the battery pack was designed in this section. The experimental test setup is depicted in Figure 16. The test equipment comprises a high-power charge and discharge system, a high- and low-temperature control box, a data acquisition system, a battery pack, a water chiller (LTF-03A-09kW, KUNSHAN LETIAN Heating and Cooling Equipment Co., Ltd. Suzhou City, China.), and a computer. The battery pack is positioned within the temperature control box. The maximum cooling capacity of the water chiller is 8.5 kW, enabling it to control the temperature of the coolant within the range of 5 °C to 35 °C. Twelve temperature acquisition points are arranged inside the battery pack, and their layout is in accordance with the positions shown in Figure 8. The temperature sensor is placed at the top surface of the battery cell, as depicted in Figure 16. The acquisition

range of the temperature sensor is -40°C to 85°C , and the acquisition accuracy is $\pm 1^{\circ}\text{C}$. The test method is as follows:

1. Connect the charge and discharge equipment and the acquisition equipment to ensure normal data acquisition. The high- and low-temperature control box adjusts the temperature to 25°C , and the battery pack temperature is left to stabilize at $25^{\circ}\text{C} \pm 2^{\circ}\text{C}$.
2. Discharge at a $1/3\text{ C}$ discharge rate until the SOC reaches 0%.
3. Adjust the temperature of the high- and low-temperature control box to 40°C . When the temperature of the battery pack reaches $40^{\circ}\text{C} \pm 2^{\circ}\text{C}$ and the temperature difference is no more than 2°C , charge it to 100% SOC in accordance with the rapid charging strategy.
4. Record data such as the charging time, the temperature of the coolant, the current, the SOC, and the temperatures at each monitoring point.

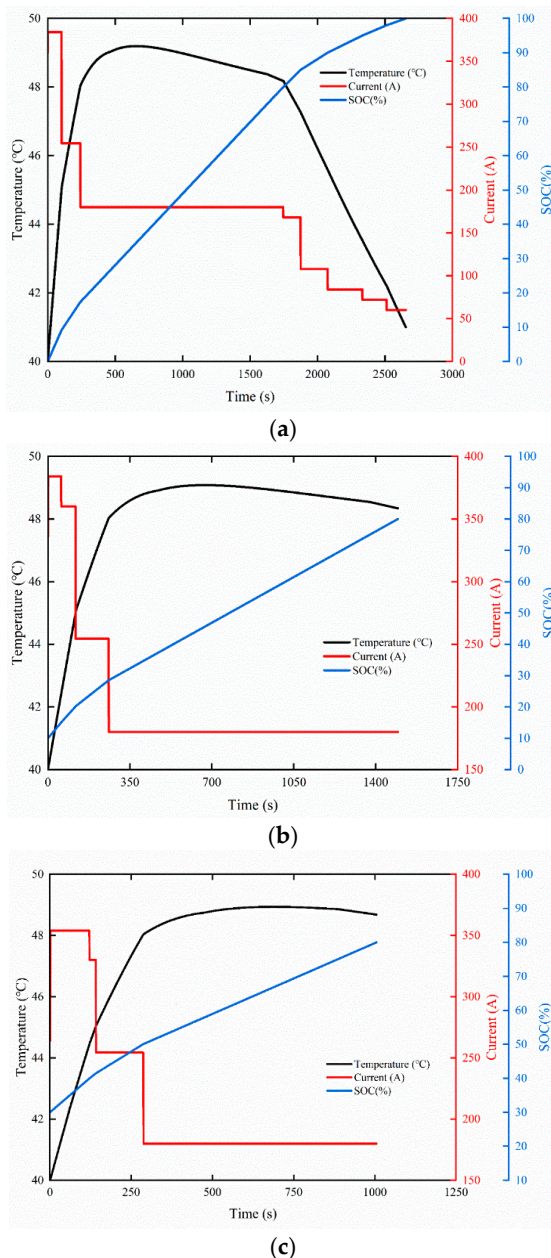


Figure 13. Comparison of charging performance at different SOC intervals based on the optimized fast charging strategy: (a) SOC: 0–100%; (b) SOC: 10–80%; (c) SOC: 30–80%.

Figure 17 presents the comparison of the experimental and simulation data of the 12 temperature acquisition points. Since the acquisition accuracy of the temperature sensor adopted in the experiment is $\pm 1^{\circ}\text{C}$, the temperature curve in Figure 17a is stepped. The temperature data measured experimentally exhibit the same variation trend as the simulation data. As depicted in Figure 17a, the experimental data indicates that the high-temperature zone of the battery is primarily concentrated in the regions where NTC1, NTC4, and NTC6 are located, and the low-temperature zone is mainly concentrated in the regions where NTC3, NTC7, NTC9, and NTC11 are located. The high- and low-temperature regions of the battery measured experimentally are in accordance with the numerical simulation results. During the experimental process, the T_{\max} of the battery collected was 49°C , and the maximum temperature difference was 5°C . Compared with the experimental data, the error of the T_{\max} in the simulation data was 0.4%, and the error of the maximum temperature difference was 5%. The entire charging process of the experiment lasted 2860 s, which was 206 s longer than the simulation time. The deviation in charging time was mainly due to the fact that the step of switching the charging rate was manually set, resulting in a certain setup time. In summary, the numerical method adopted in this research is reliable.

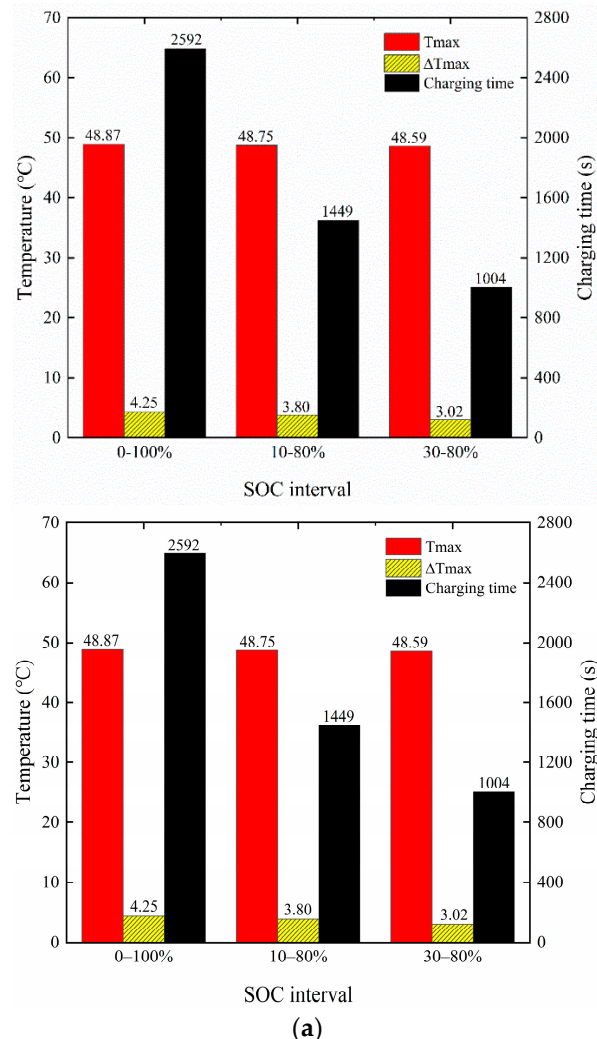


Figure 14. Cont.

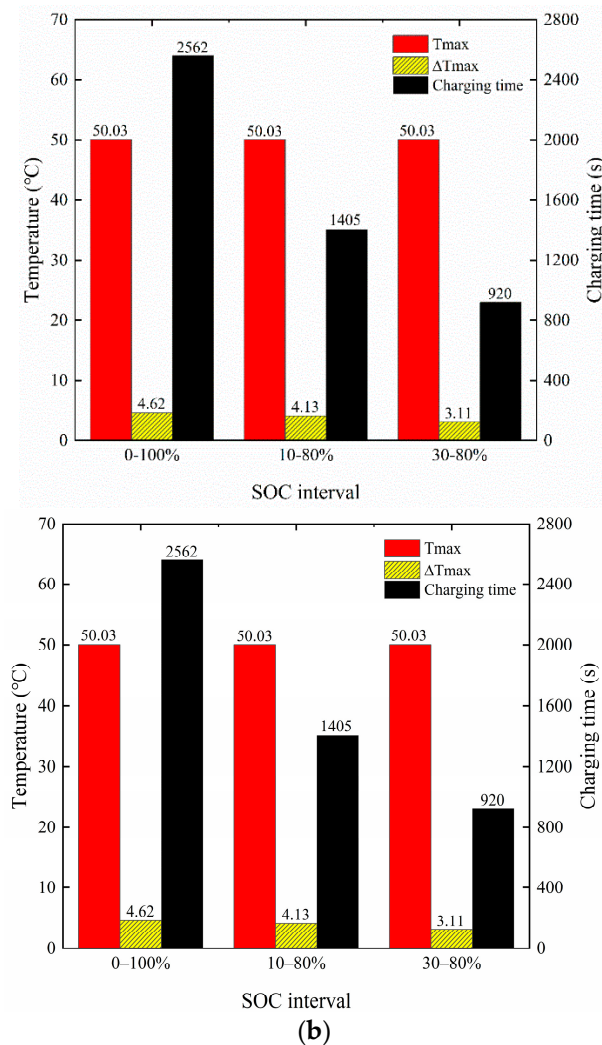


Figure 14. Comparison of charging performance under different charging strategies at a cooling strategy of $20\text{ }^{\circ}\text{C}$ @12 L/min: (a) optimization strategy; (b) original strategy.

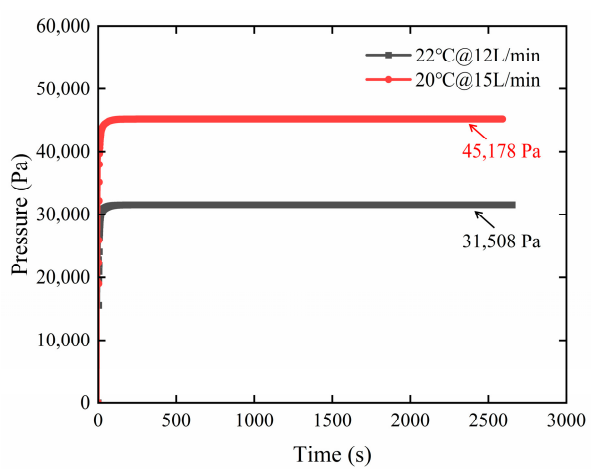


Figure 15. Comparison of system pressure drop under different cooling strategies.

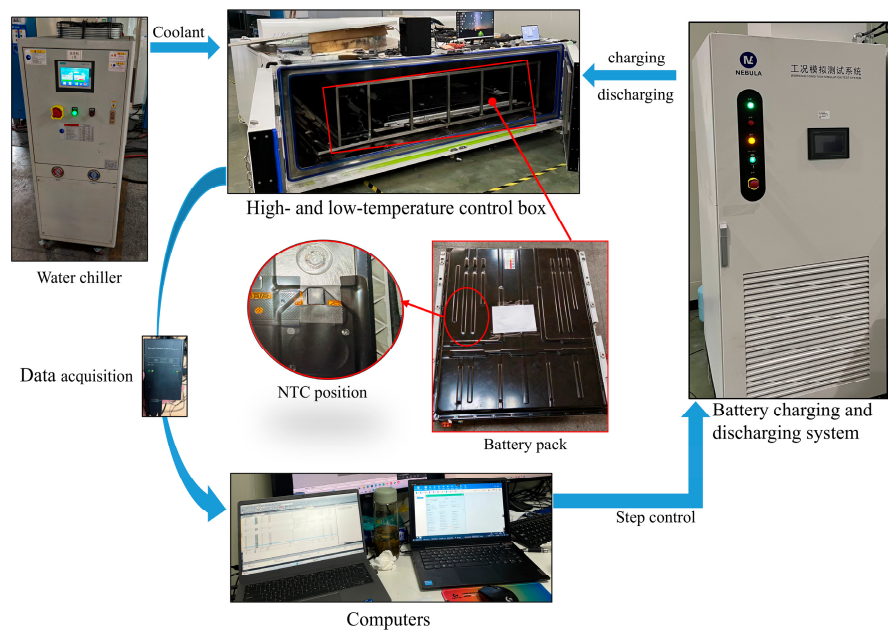


Figure 16. Battery pack charging test system.

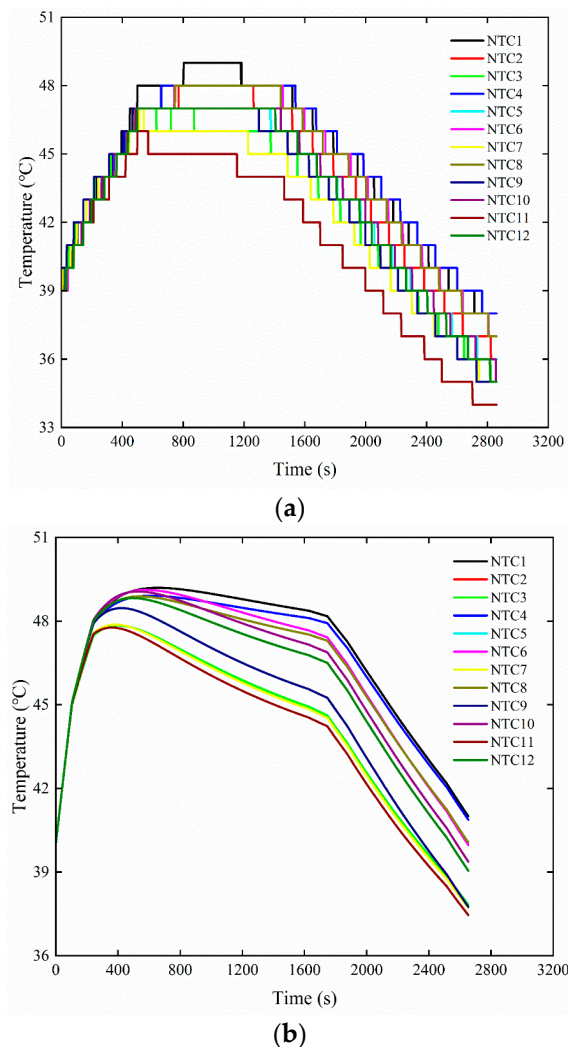


Figure 17. Comparison of NTC temperature during charging process: (a) experimental results; (b) numerical results.

4. Conclusions

In this study, a heat generation model of the battery was established through HPPC tests. The charging model under high ambient temperature for the battery was constructed by combining the fast charging strategy and the cooling strategy. By investigating the influence of the cooling strategy on the charging performance, an optimization strategy of limiting the charging rate within the high-temperature range was proposed. The main conclusions are as follows.

A fast charging strategy regulated based on battery state of charge (SOC) and temperature gives full play to the maximum charging capacity of the cell. It takes 2634 s to charge the battery from 0% to 100% SOC, and the T_{max} of the battery throughout the charging process is 50.04 °C.

Increasing the inlet flow rate can shorten the charging time of the battery, but at the expense of the pressure drop of the liquid cooling system. When the inlet flow rate is increased from 12 L/min to 15 L/min, the charging time is reduced by 25 s, but the pressure drop of the liquid cooling system rises by 44%. Furthermore, reducing the inlet coolant temperature can significantly enhance the charging efficiency. When the inlet coolant temperature is decreased to 20 °C, the entire charging process lasts for 2585 s, but the T_{max} of the battery does not improve.

To reduce the T_{max} of the battery during the charging process, the charging rate within the high-temperature range was optimized on the basis of the original fast charging strategy. Based on the optimized fast charging strategy, the T_{max} during the process of charging the battery from 0% to 100% SOC was 49.19 °C.

Author Contributions: Conceptualization, Q.Z.; methodology, Q.Z. and Y.Y.; software, Q.Z. and Y.Y.; validation, Y.Y.; investigation, Q.Z. and Y.Y.; resources, Q.Z.; data curation, Q.Z.; writing—original draft preparation, Q.Z.; writing—review and editing, Q.Z.; visualization, Y.Y.; supervision, Q.Z.; project administration, Q.Z.; funding acquisition, Q.Z. All authors have read and agreed to the published version of the manuscript.

Funding: This research was funded by the Key Project of Natural Science Research in Anhui Province's Universities, grant number 2023AH051712.

Data Availability Statement: Data generated or analyzed during this study are included in this published article.

Conflicts of Interest: The authors declare no conflicts of interest.

References

1. Potiwan, P.; Pothiwan, M.; Yuan, X.M.; Bamroongboon, K. Next generation vehicles: Status quo in Southeast Asia. *Int. J. Global Warm.* **2022**, *28*, 60–80. [[CrossRef](#)]
2. Witsarut, A.; Pana, S.; Sarunnoud, P.; Yuttana, M.; Ramnarong, W.; Panuwat, P. Potential reductions of CO₂ emissions from the transition to electric vehicles: Thailand's scenarios towards 2030. *Energy Rep.* **2023**, *9*, 124–130.
3. Veza, I.; Abas, M.A.; Djamarai, D.W.; Tamaldin, N.; Endrasari, F.; Budiman, B.A.; Idris, M.; Opia, A.C.; Juangsa, F.B.; Aziz, M. Electric Vehicles in Malaysia and Indonesia: Opportunities and Challenges. *Energies* **2022**, *15*, 2564. [[CrossRef](#)]
4. Ahmad, A.; Roger, D.; Ariel, L.; Gawler, R. Integration of Electric Vehicles and Renewable Energy in Indonesia's Electrical Grid. *Energies* **2024**, *17*, 2037. [[CrossRef](#)]
5. Roy, N.; Kumar, K.S.; Raju, B.D.; Karami, A.M.; Reddy, G.R.; Barai, H.R.; Joo, S.W. Influence of metal cations on 3D MCoMnO₄ microstructures (M = Ni and Zn) for battery-type supercapacitors: A comprehensive study. *Colloid. Surface A* **2024**, *685*, 133240. [[CrossRef](#)]
6. Steinhardt, M.; Barreras, J.V.; Ruan, H.J.; Wu, B.; Offer, G.J.; Jossen, A. Meta-analysis of experimental results for heat capacity and thermal conductivity in lithium-ion batteries: A critical review. *J. Power Sources* **2022**, *522*, 230829. [[CrossRef](#)]
7. Liu, Z.; Wang, B.; Chen, S.; Li, P. Lithium-ion battery pack thermal management under high ambient temperature and cyclic charging-discharging strategy design. *J. Energy Storage* **2024**, *80*, 110391. [[CrossRef](#)]

8. Yu, C.; Huang, S.; Xu, H.; Yan, J.; Rong, K.; Sun, M. Optimal charging of lithium-ion batteries based on lithium precipitation suppression. *J. Energy Storage* **2024**, *82*, 110580. [[CrossRef](#)]
9. Chavan, S.; Venkateswarlu, B.; Salman, M.; Liu, J.; Pawar, P.; Choi, G.S.; Kim, S.C. Thermal management strategies for lithium-ion batteries in electric vehicles: Fundamentals, recent advances, thermal models, and cooling techniques. *Int. J. Heat. Mass. Tran.* **2024**, *232*, 125918. [[CrossRef](#)]
10. Tang, A.K.; Yang, J.Z.; Yang, P.; Zhang, H.; Cai, T. Optimization and working performance analysis of liquid cooling plates in refrigerant direct cooling power battery systems. *Int. J. Heat. Mass. Tran.* **2024**, *231*, 125899. [[CrossRef](#)]
11. Zhang, B.X.; Yuan, N.L.; Kong, B.B.; Zou, Y.T.; Shi, H. Simulation of hybrid air-cooled and liquid-cooled systems for optimal lithium-ion battery performance and condensation prevention in high-humidity environments. *Appl. Therm. Eng.* **2024**, *257*, 124455. [[CrossRef](#)]
12. Kang, Y.J.; Hu, Y.P.; Zhang, C.H.; Yang, K.; Zhang, Q. Experimental study on charge amount of low-GWP refrigerants in electric vehicle thermal management system. *Appl. Therm. Eng.* **2024**, *256*, 124059. [[CrossRef](#)]
13. Zhao, G.; Wang, X.L.; Negnevitsky, M.; Li, C.J. An up-to-date review on the design improvement and optimization of the liquid-cooling battery thermal management system for electric vehicles. *Appl. Therm. Eng.* **2024**, *219*, 119626. [[CrossRef](#)]
14. Guo, R.; Li, L. Heat dissipation analysis and optimization of lithium-ion batteries with a novel parallel-spiral serpentine channel liquid cooling plate. *Int. J. Heat. Mass. Tran.* **2022**, *189*, 122706. [[CrossRef](#)]
15. Zhao, D.; Lei, Z.; An, C. Research on battery thermal management system based on liquid cooling plate with honeycomb-like flow channel. *Appl. Therm. Eng.* **2023**, *218*, 119324. [[CrossRef](#)]
16. Kewalramani, G.V.; Agrawal, A.; Saha, S.K. Modeling of microchannel heat sinks for electronic cooling applications using volume averaging approach. *Int. J. Heat. Mass. Tran.* **2017**, *115*, 395–409. [[CrossRef](#)]
17. Fan, Y.; Wang, Z.; Fu, T.; Wu, H. Numerical investigation on lithium-ion battery thermal management utilizing a novel tree-like channel liquid cooling plate exchanger. *Int. J. Heat. Mass. Tran.* **2022**, *183*, 122143. [[CrossRef](#)]
18. Luo, T.; Wang, Q.; Dai, L.; Dang, X.; He, Z.; Ji, H. Numerical studies on topological design of cold plate for a cell-to-pack battery system. *Appl. Therm. Eng.* **2024**, *244*, 122715. [[CrossRef](#)]
19. He, P.; Lu, H.; Fan, Y.; Ruan, H.; Wang, C.; Zhu, Y. Numerical investigation on a lithium-ion battery thermal management system utilizing a double-layered I-shaped channel liquid cooling plate exchanger. *Int. J. Therm. Sci.* **2023**, *187*, 108200. [[CrossRef](#)]
20. Mao, S.; Han, M.; Han, X.; Lu, L.; Feng, X.; Su, A.; Wang, D.; Chen, Z.; Lu, Y.; Ouyang, M. An Electrical–Thermal Coupling Model with Artificial Intelligence for State of Charge and Residual Available Energy Co-Estimation of LiFePO₄ Battery System under Various Temperatures. *Batteries* **2022**, *8*, 140. [[CrossRef](#)]
21. Gao, T.F.; Bai, J.L.; Ouyang, D.X.; Wang, Z.R.; Bai, W.; Mao, N.; Zhu, Y. Effect of aging temperature on thermal stability of lithium-ion batteries: Part A-High-temperature aging. *Renew. Energy* **2023**, *203*, 592–600. [[CrossRef](#)]
22. Sheng, L.; Zhang, C.F.; Xu, J.; Zhang, X.J.; Wang, X.Y.; Zhang, Z.D. In-situ characterization approach for heat-generating performances of a pouch lithium-ion battery. *Appl. Therm. Eng.* **2024**, *256*, 124081. [[CrossRef](#)]
23. Same, J.S.; El-Tayeb, A.; Moukhtar, I.; Abdelhameed, E.H.; El-Dein, A.Z. Effect of Thermal Parameters on Behaviour of a Lithium-Ion Battery: Simulation Study. *Int. J. Electrochem. Sc.* **2022**, *17*, 220951. [[CrossRef](#)]
24. Hwang, S.; Choi, R.; Kim, S.; Song, M.; Kim, T. Numerical analysis of LiFePo₄ battery thermal management system using cold plate. *J. Mech. Sci. Technol.* **2023**, *37*, 3163–3171. [[CrossRef](#)]
25. de Parga-Regalado, A.M.A. Analytical approximation of optimal thermoeconomic efficiencies for a Novikov engine with a Stefan–Boltzmann heat transfer law. *Results Phys.* **2023**, *54*, 107059. [[CrossRef](#)]
26. Zhao, J.; Chu, D.; Yang, X.; Zhang, W.; Kang, B. Study on thermal model of thermal battery. *Chin. J. Power Sources* **2008**, *32*, 614–616.
27. Shen, K.; Chen, L.; Feng, X.; Zheng, Y.; Sun, Y.; Xu, C.; Wang, H.; Jin, C.; Han, X.; Lai, X.; et al. Non-destructive battery fast charging constrained by lithium plating and high temperature limit based on simulation. *J. Energy Storage* **2024**, *84*, 110896. [[CrossRef](#)]
28. Landini, S.; O’Donovan, T.S. Novel experimental approach for the characterisation of Lithium-Ion cells performance in isothermal conditions. *Energy* **2021**, *214*, 118965. [[CrossRef](#)]
29. Xie, W.; Guo, P.; Gao, X. Elucidating the rate limitation of lithium-ion batteries under different charging conditions through polarization analysis. *J. Energy Storage* **2024**, *82*, 110554. [[CrossRef](#)]
30. Trinuruk, P.; Onnuam, W.; Senanuch, N.; Sawatdeejui, C.; Jenyongsak, P.; Wongwises, S. Experimental and Numerical Studies on the Effect of Lithium-Ion Batteries’ Shape and Chemistry on Heat Generation. *Energies* **2023**, *16*, 264. [[CrossRef](#)]
31. Lin, B.Q.; Yang, M.Q. Changes in consumer satisfaction with electric vehicle charging infrastructure: Evidence from two cross-sectional surveys in 2019 and 2023. *Energ Policy* **2024**, *185*, 113924. [[CrossRef](#)]